



JGR Space Physics

RESEARCH ARTICLE

10.1029/2024JA032538

Key Points:

- Harmonics of Magnetosonic wave are observed in the Martian magnetosphere in dawn sector (5–10 LT)
- Magnetosonic harmonics dominantly have right-handed polarization
- Ambient proton density and velocity found to vary with fundamental mode frequency of 46 mHz

Correspondence to:

B. Kakad, bharati.kakad@iigm.res.in

Citation:

Kakad, B., Kakad, A., Omura, Y., & Yoon, P. H. (2024). First observation of harmonics of magnetosonic waves in Martian magnetosheath region. *Journal of Geophysical Research: Space Physics*, 129, e2024JA032538. https://doi.org/10.1029/2024JA032538

Received 11 FEB 2024 Accepted 26 JUN 2024

Author Contributions:

Conceptualization: Amar Kakad Formal analysis: Bharati Kakad Project administration: Amar Kakad Resources: Yoshiharu Omura, Peter H. Yoon

Validation: Peter H. Yoon Visualization: Yoshiharu Omura, Peter

Writing - original draft: Bharati Kakad

Software: Amar Kakad

Writing – review & editing: Amar Kakad, Yoshiharu Omura, Peter H. Yoon

© 2024. American Geophysical Union. All Rights Reserved.

First Observation of Harmonics of Magnetosonic Waves in Martian Magnetosheath Region

Bharati Kakad¹, Amar Kakad¹, Yoshiharu Omura², and Peter H. Yoon³

¹Indian Institute of Geomagnetism, New Panvel, Navi Mumbai, India, ²Research Institute for Sustainable Humanosphere, Kyoto University, Kyoto, Japan, ³Institute for Physical Science and Technology, University of Maryland, College Park, MD, USA

Abstract The present study provides an evidence for the generation of harmonics of magnetosonic waves in the Martian magnetosheath region. The wave signatures are manifested in the magnetic field measurements recorded by the fluxgate magnetometer instrument onboard the Mars Atmosphere and Volatile Evolution missioN (MAVEN) spacecraft in the dawn sector around 5–10 LT at an altitude of 4,000–6,000 kms. The wave that is observed continuously from 19.1 to 20.7 UT below the proton cyclotron frequency ($f_{ci} \approx 46$ mHz) is identified as fundamental mode of the magnetosonic wave. Whereas harmonics of the magnetosonic wave are observed during 19.7–20.3 UT at frequencies that are multiple of f_{ci} . The ambient solar wind proton density and plasma flow velocity are found to vary with a fundamental mode frequency of 46 mHz. It is noticed that the fundamental mode is mainly associated with the left-hand (LH), and higher frequency harmonics are associated with the right-hand (RH) circular polarizations. A clear difference in the polarization and ellipticity is noticed during the time of occurrence of harmonics. The magnetosonic wave harmonics are found to propagate in the quasi-perpendicular directions to the ambient magnetic field. The results of linear theory and Particle-In-Cell simulation performed here are in agreement with the observations. The present study provides a conclusive evidence for the occurrence of harmonics of magnetosonic wave in the close vicinity of the magnetosheath region of the unmagnetized planet Mars.

Plain Language Summary Mars is an unmagnetized planet. The solar wind particles that bombard Mars continuously, are responsible for the loss of its atmosphere. This scenario is opposite to that of the Earth, as its strong intrinsic magnetic field forms a protective shield around the planet, called the magnetosphere. Various electrostatic/electromagnetic waves are often generated in the Earth's magnetosphere, which are potential candidates for controlling the transfer of energy and momentum from one region to another. In case of Mars, it possesses a weakly induced magnetosphere, which is dynamic due to its continuous interactions with solar wind. The field measurements from the MAVEN spacecraft can be used to understand plasma waves in the vicinity of Mars. Here, we report the first observations of the harmonics of magnetosonic wave in the Martian magnetosheath region. The magnetosonic waves are low-frequency compressive waves driven by the ions in the presence of magnetic field. These waves are known to play a role in the particle heating process in the Earth's magnetosphere. Therefore, its observation in the Martian plasma environment is of interest to the scientific community to understand their role in plasma heating in the Martian ionosphere-magnetosphere system.

1. Introduction

The collisionless plasma in the Earth's magnetosphere exhibits a wide variety of wave modes that are classified according to their frequency, polarization characteristics, types of oscillation (longitudinal or transverse), and their dispersion relations. Among these, the magnetosonic waves refer to the intense electromagnetic emissions with frequencies in the range of the proton gyrofrequency to the lower hybrid resonance frequency. They have been widely observed by several spacecraft and are known as one of the candidates for playing a fundamental role in the energy transfer process in different regions of Earth's magnetosphere (Leonovich & Kozlov, 2013). The observational and theoretical investigations indicate that a natural instability linked to a ring-type distribution of energetic protons can excite magnetosonic waves that propagate in quasi-perpendicular direction with respect to the ambient magnetic field vector (Chen et al., 2011; Meredith et al., 2008; Teng, Liu, et al., 2021). The observations have also demonstrated the occurrence of harmonics of magnetosonic waves having frequency in multiples of proton gyrofrequency and the upper frequency limit is provided by the lower hybrid frequency (Balikhin et al., 2015; Huang et al., 2020).

KAKAD ET AL. 1 of 14

Recent planetary missions have opened up an opportunity to probe plasma waves and instabilities in the planetary environments. In particular, the plasma environment of the unmagnetized planet such as Mars has prompted a growing interest in investigating the type of plasma waves and their role in particle dynamics supported in the Martian ionosphere-magnetosphere system. It is the second planet after Earth, which has been most explored remotely by spacecraft. Mars lacks a strong, intrinsic magnetic field, which leaves its upper atmosphere vulnerable to the solar wind creating induced magnetic cavity with distinct regions, including a bow shock, magnetosheath, and thin magnetosphere. Under such conditions, the dynamics of plasma waves and their effects on the Martian magnetospheric plasma are expected to be different from those in the Earth's magnetosphere. The study of plasma waves on Mars has garnered interest in recent times because of its possible influence on the plasma heating and loss in the Martian upper atmosphere (Ergun et al., 2006, 2016; Fowler et al., 2020). The electron Landau heating by magnetosonic waves is proposed as a new mechanism for the Martian ionospheric erosion (Su et al., 2020). Hence, it is currently necessary to comprehend the underlying physical mechanism for wave formation and their role in particle dynamics in the Martian magnetosphere.

Spacecraft missions have revealed the complexity and dynamic nature of the Martian magnetosphere (DiBraccio et al., 2018; Halekas et al., 2017). Consequently, there is a growing interest in identifying and comprehending each channel of energy flows carried by particles and fields in and around the Martian near space. For instance, recent observations from Mars Atmosphere and Volatile Evolution (MAVEN) observed different classes of electrostatic and electromagnetic waves in Martian magnetosphere. For example, the electrostatic solitary waves are observed in the Martian magnetosheath region (B. Kakad et al., 2022). A recent study by A. Kakad et al. (2023) reported observations of two distinct wave modes with frequency below and above the electron plasma frequency. Besides these waves, the electron-induced whistler mode waves (Harada et al., 2016), lower-hybrid waves (Guo et al., 2022) and ultra-low frequency electromagnetic waves (Harada et al., 2019) are also observed in the Martian magnetosphere by making use of MAVEN spacecraft.

Recently, there has been growing attention toward probing magnetosonic waves in the Martian plasma environment due to their potential role in Martian ionospheric erosion through heating the ionospheric plasma (Collinson et al., 2018; Fowler et al., 2018, 2020). Earlier studies have reported the magnetosonic waves in the Martian plasma environment. However, most of these reports are in the ionospheric region (Bertucci et al., 2004; Collinson et al., 2018; Espley et al., 2004; Fowler et al., 2018; Halekas et al., 2011; Wang et al., 2023). A recent study has shown the presence of magnetosonic wave in the magnetotail region around 2,000–3,000 kms (Teng et al., 2024). However, the harmonics of magnetosonic waves in the Martian environment have not been reported so far, in contrast to the Earth's magnetosphere where it is a common occurrence (Balikhin et al., 2015). We present here the first observation of a series of harmonics of magnetosonic waves in the Martian magnetosphere. Making use of the Particle-In-Cell (PIC) simulations and theory, we have confirmed the generation scenario of such harmonics of magnetosonic waves in the high plasma beta environment, which characterizes the Martian magnetosheath region. It may be noted that the magnetosonic waves reported here are not the "magnetosonic" mode from the magnetohydrodynamic theory that propagates well below the ion cyclotron frequency (Santolík et al., 2016). Gary et al. (2010) explained that magnetosonic waves more properly should be referred as the ion Bernstein waves. In this article we use the commonly used nomenclature from the literature that is, magnetosonic waves.

The organization of the present paper is as follows: The paper begins by providing the information related to the data used in the present study, which is given in Section 2. The observation and simulation results are presented and discussed in Section 3. The conclusions drawn from the study are summarized in Section 4.

2. Data Information

The MAVEN mission provides an excellent opportunity to explore the plasma processes in the vicinity of Mars through high-resolution particle and field measurements. The MAVEN spacecraft carried onboard a number of different payloads, for example, Langmuir Probe and Waves, Solar Wind Electron Analyzer (SWEA), and Solar Wind Ion Analyzer (SWIA), from which one may collect ion flux data, etc (Andersson et al., 2015; Halekas et al., 2015; Mitchell et al., 2016). These instruments measure electric field and electron and ion particle fluxes, and in the present study, we have also made use of the vector magnetic field data acquired by the fluxgate magnetometer instrument on the MAVEN spacecraft. The magnetic field data are calibrated and provided in units of nano-Tesla. The time resolution of magnetic field measurement is one second. The data are recorded in Sun

KAKAD ET AL. 2 of 14

21699402, 2024, 7, Downloaded from https://agupubs.onlinelibrary.wiley.com/doi/10.1029/2024JA032538 by University Of California - Berkeley, Wiley Online Library on [14/07/2024]. See the Terms and Conditions (https://agupubs.onlinelibrary.wiley.com/doi/10.1029/2024JA032538 by University Of California - Berkeley, Wiley Online Library on [14/07/2024]. See the Terms and Conditions (https://agupubs.onlinelibrary.wiley.com/doi/10.1029/2024JA032538 by University Of California - Berkeley, Wiley Online Library on [14/07/2024]. See the Terms and Conditions (https://agupubs.onlinelibrary.wiley.com/doi/10.1029/2024JA032538 by University Of California - Berkeley, Wiley Online Library on [14/07/2024]. See the Terms and Conditions (https://agupubs.onlinelibrary.wiley.com/doi/10.1029/2024JA032538 by University Of California - Berkeley, Wiley Online Library on [14/07/2024]. See the Terms and Conditions (https://agupubs.onlinelibrary.wiley.com/doi/10.1029/2024JA032538 by University Of California - Berkeley, Wiley Online Library on [14/07/2024]. See the Terms and Conditions (https://agupubs.onlinelibrary.wiley.com/doi/10.1029/2024JA032538 by University Of California - Berkeley, Wiley Online Library on [14/07/2024]. See the Terms and Conditions (https://agupubs.onlinelibrary.wiley.com/doi/10.1029/2024JA032538 by University Of California - Berkeley, Wiley Online Library on [14/07/2024]. See the Terms and Conditions (https://agupubs.onlinelibrary.wiley.com/doi/10.1029/2024JA03258 by University Of California - Berkeley, Wiley Online Library on [14/07/2024]. See the Terms and Conditions (https://agupubs.onlinelibrary.wiley.com/doi/10.1029/2024JA03258 by University Of California - Berkeley, Wiley Online Library on [14/07/2024]. See the Terms and Conditions (https://agupubs.onlinelibrary.wiley.com/doi/10.1029/2024JA03258 by University Online Library.wiley.com/doi/10.1029/2024JA03258 by University Online Library.wiley.com/doi/10.1029/2024JA03258 by University Online Library.wiley.com/doi/10.1029/2024JA03258 by University Online Library.

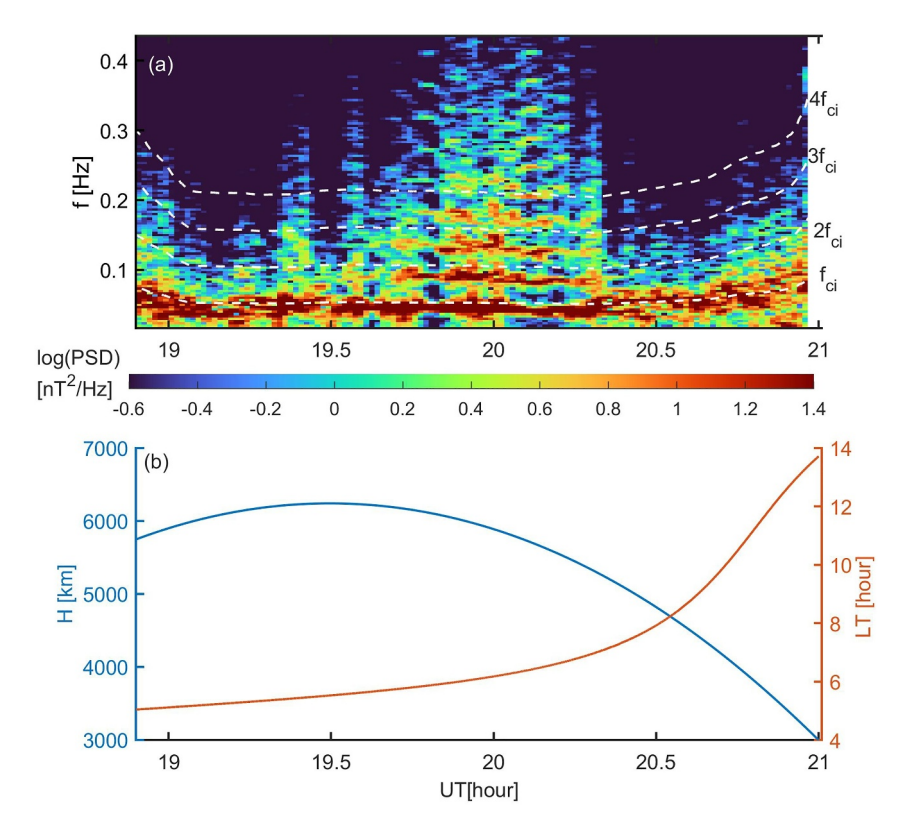


Figure 1. Top panel (a) shows the spectrogram of the total magnetic field on 21 February 2015, during 19.1–20.7 UT. The color scale shows the power spectral density of the total magnetic field in units of nT^2/Hz . The horizontal white dashed lines indicate the multiples of local proton gyro-frequency at f_{ci} , $2f_{ci}$, $3f_{ci}$, and $4f_{ci}$. The continuous wave activity below proton gyro-frequency is identified as fundamental mode of magnetosonic wave. While the multiple higher frequency modes are identified as magnetosonic wave harmonics. Lower panel (b) Shows the variation of altitude (blue color) and local time (red color) of MAVEN spacecraft during the observation of these low-frequency waves.

State coordinate system (Connerney et al., 2015). The calibrated key parameters, such as density, temperature, solar wind velocity, altitude, local time, etc., derived from various instruments mounted on MAVEN, are used to determine the ambient plasma conditions in the observation region. These derived key parameters are available at 4 s or 8 s resolution and can be downloaded from https://pds-ppi.igpp.ucla.edu. In the next section, we discuss the results of analysis based on these data.

3. Results and Discussion

On 21 February 2015, the magnetosonic wave and its harmonics are observed in the magnetosheath region of the Mars. The three-dimensional magnetic field strength measured by the fluxgate magnetometer on board the MAVEN spacecraft reveals the signature of magnetosonic wave. These observations and their characteristics are discussed in the following subsections.

3.1. Magnetosonic Wave Observations

Figure 1a shows the spectrogram of the total magnetic field on 21 February 2015, during 19.1–20.7 UT. The sampling of the magnetic field is one second. We took three-dimensional magnetic field data, $[B_x(t), B_y(t), B_z(t)]$, in the sun-state coordinate system and obtained power spectral densities, $[P_x(f, t), P_y(f, t), P_z(f, t)]$ by performing a one-dimensional Fourier transform using a window of 300 s with an overlap of 80%. The power spectral density of the total magnetic field is estimated as $P(f, t) = P_x(f, t) + P_y(f, t) + P_z(f, t)$ in units of P^2 Hz. The resolution of the spectrogram is 60 s and 3.3 mHz in the time and frequency domains, respectively. The color scale in Figure 1a represents the power spectral density. The horizontal white dashed lines indicate the multiples of local proton gyro-frequency at P_{ci} , P_{ci} , P_{ci} , P_{ci} , and P_{ci} . During 19.1–20.7 UT, it can be seen that the wave power around and

KAKAD ET AL. 3 of 14

21699402, 2024, 7, Downloaded from https://agupubs. onlinelibrary.wiley.com/doi/10.1029/2024JA032538 by University Of California - Berkeley, Wiley Online Library on [14/07/2024]. See the Terms and Conditional Conditions of California - Berkeley, Wiley Online Library on [14/07/2024]. See the Terms and Conditional Conditional Conditions of California - Berkeley, Wiley Online Library on [14/07/2024]. See the Terms and Conditional Conditional Conditions of California - Berkeley, Wiley Online Library on [14/07/2024]. See the Terms and Conditional Conditiona

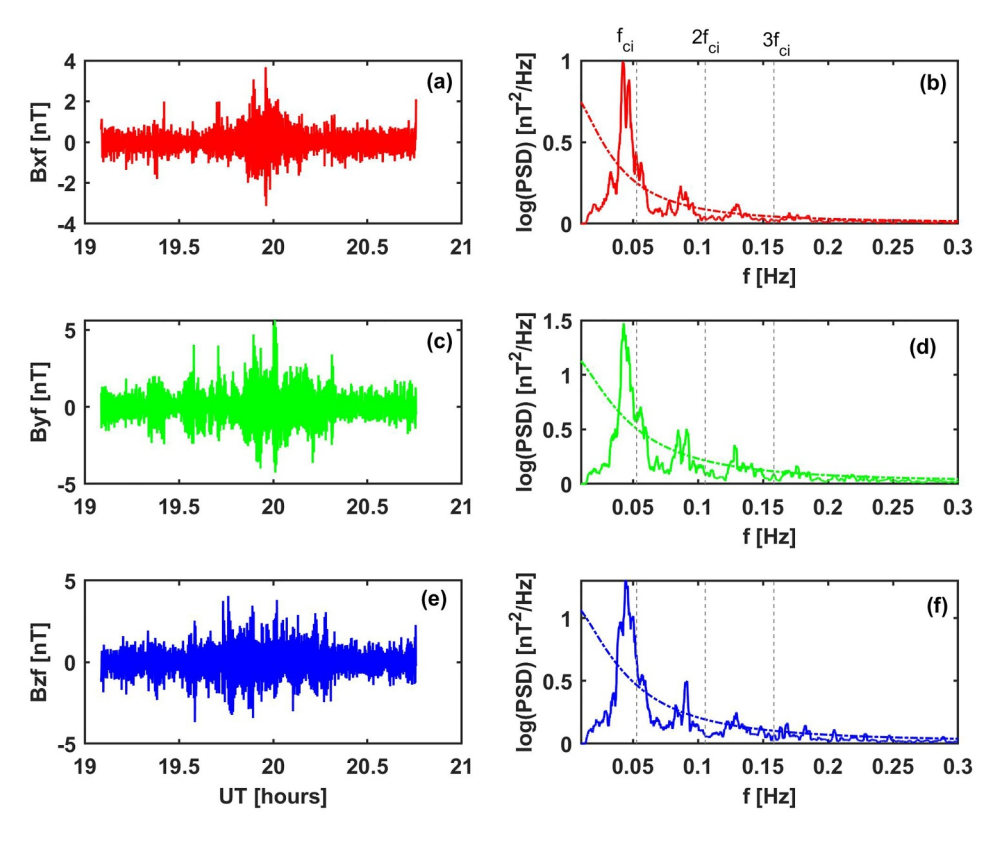


Figure 2. Panels (a, c, e) show the filtered x, y, and z components of the magnetic field, respectively, and panels (b, d, f) show their respective Fourier transform spectra. The dashed-dotted lines in the right-side panels indicate the 90% statistical significance level, and the vertical dashed lines indicate the multiples of proton gyro-frequency at f_{ci} , $2f_{ci}$, and $3f_{ci}$.

slightly below frequency f_{ci} is rather high and its intensity is continuously maintained over the entire time period. Additionally, during 19.7–20.3 UT, harmonics are seen between f_{ci} = $2f_{ci}$, $2f_{ci}$ = $3f_{ci}$, and $3f_{ci}$ = $4f_{ci}$.

The continuous wave activity below proton gyro-frequency looks like Electromagnetic Ion Cyclotron (EMIC) wave. However, when Doppler shift is estimated, it is identified as the fundamental mode of the magnetosonic wave, while the multiple higher frequency waves are identified as the harmonics of the magnetosonic wave. The identification of these waves are based on the Doppler shift, polarization, ellipticity, and wave normal angle, which is discussed in the next subsection. The proton gyro-frequency is around 46 mHz (i.e., 22 s). Figure 1b shows the variation of altitude (blue color) and local time (red color) of MAVEN spacecraft during the wave observation. It is noticed that this wave event is captured by the spacecraft in the dawn sector around 5–10 LT at altitudes of 4,000–6,000 km.

We have also checked the Fourier transform of individual components of the magnetic field to verify the presence of these low-frequency waves in the data. The filtered x, y, and z components of the magnetic field are shown in Figures 2a, 2c, and 2e, respectively, and their respective Fourier transformed spectra are plotted in Figures 2b, 2d, and 2f. The dashed-dotted lines in the right-hand panels of Figure 2 indicate the 90% statistical significance level, and the vertical dashed lines indicate the multiples of proton gyro-frequency at f_{ci} , $2f_{ci}$, and $3f_{ci}$. One can see that the harmonics of magnetosonic wave are evident in each component of the magnetic field.

The ions and ambient magnetic field play an important role in the generation of the magnetosonic wave—therefore, we examined the variation of proton density and solar wind velocity during the event. The proton density and velocity are derived from the SWIA instrument on MAVEN, and these observations are available at 4 s sampling. We know that the solar wind velocity represents the ion flow, mainly of that of the protons. The ion density and three components of the solar wind velocity vector are plotted in Figures 3a and 3c, and their respective Fourier spectra are shown in Figures 3b and 3d, respectively. The dashed-dotted lines in the right-hand panels of Figure 3 show 90% statistical significance. It is clearly seen that the fundamental frequency of 46 mHz is

KAKAD ET AL. 4 of 14

rom https://agupubs.onlinelibrary.wiley.com/doi/10.1029/2024JA032538 by University Of California - Berkeley, Wiley Online Library on [14/07/2024]. See the

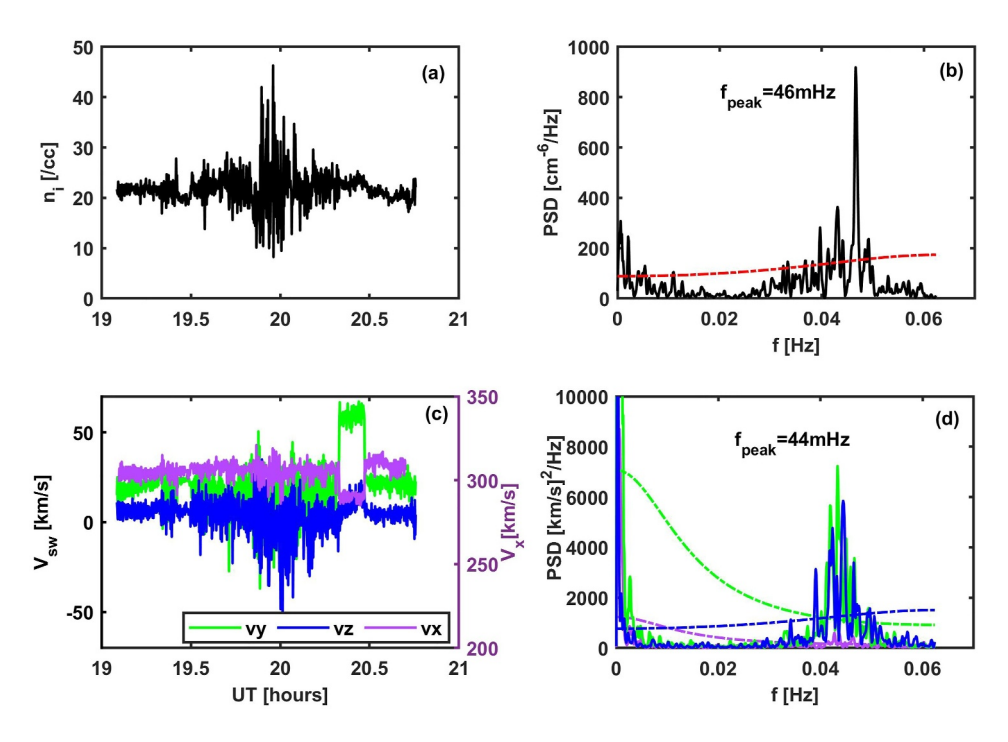


Figure 3. The variation of (a) proton density and (c) solar wind velocity derived from the SWIA instrument on MAVEN are plotted for the event duration. The data is available for 4 s resolution. The Fourier spectra of ion density and velocity are shown in panels (b, d), respectively. The dashed-dotted lines in the right-hand panels indicate 90% statistical significance. The fundamental frequency of 46 mHz is dominantly seen in ion density and the y and z components of the solar wind velocity.

dominantly present in the ion density and the y and z components of the solar wind velocity. This frequency match with the fundamental mode suggests that the plasma density and velocity fluctuations are part of the observed magnetosonic waves.

Here, we discuss about the Doppler shift. Teng et al. (2024) have reported the magnetosonic wave from the Martian magnetotail region in the nightside sector. While interpreting these wave observations the authors have estimated the Doppler shift by following Jian et al. (2010), and found that the Doppler shift effects due to ion bulk velocity are not significant due to small values of the ion bulk flow. We have adopted the same method and computed the Doppler shift for the magnetosonic wave observed in the dawn to morning sector, where the solar wind ion flows are stronger. The general formula for the Doppler shift is as follows,

$$f_{actual} = \frac{(V_{wave} + V_{source}) \times f_{observed}}{(V_{wave} + V_{observer})} \tag{1}$$

Here, f_{actual} is the actual wave frequency, V_{wave} is wave speed (taken as Alfven wave speed 14 km/s), $f_{observed}$ is observed wave frequency, $V_{observer}$ is speed of observer (i.e., satellite velocity 4 km/s) and V_{source} is the source velocity. The source velocity is the solar wind flow velocity component along the direction of the wave propagation that is, $V_{sw}\cos(\theta)$, where θ is considered as 85–89° (see Section 3.2) for quasi perpendicular propagation. The satellite speed is smaller as compared to the wave speed. The calculations using Equation 1 suggest that the observed wave might be Doppler shifted with a factor of 1.1–2.2. It means the actual frequency could be 1.1 to 2.2 times that of the observed frequency in the spectrogram (see Figure 1). In such a scenario, the wave mode below f_{ci} is identified as fundamental mode of the magnetosonic wave.

3.2. Polarization and Ellipticity Characteristics

In this section, we discuss the polarization, ellipticity, and wave vector characteristics of the magnetosonic waves observed in the Martian magnetosphere. We have obtained this information following the method described in earlier study (B. Kakad et al., 2018). In order to estimate the polarization of the wave (i.e., right-handed or left-

KAKAD ET AL. 5 of 14

handed), one can check the rotation of the perpendicular wave vector $(B_{w\perp})$ with respect to the parallel wave vector $(B_{w\parallel})$. The parallel wave direction is considered as the direction of the ambient magnetic field (B_0) . If we let $B_w = [B_{wx}, B_{wy}, B_{wz}]$ be the wave vector, and $B_0 = [B_{0x}, B_{0y}, B_{0z}]$ be the ambient magnetic field, then it follows that the parallel and perpendicular components of the wave can be estimated making use of the following equations:

$$\vec{B}_{w\parallel} = \begin{bmatrix} \vec{B}_w \cdot \vec{B}_0 \\ \vec{B}_0 \end{bmatrix} \frac{\vec{B}_0}{|\vec{B}_0|}$$
 (2)

$$\vec{B}_{w\perp} = \vec{B}_w - \vec{B}_{w\parallel} \tag{3}$$

Further, we have estimated the cross product of the vectors $\vec{B}_{w\perp}$ at time t and $\vec{B}_{w\perp}$ at time $t + \Delta t$, and termed it as \vec{R} . Here, Δt is taken as T/4, where T=22 s, is the wave period of fundamental mode. It may be noted that, as an example, we have taken T as the period of the fundamental mode; however we have carried out this analysis for each magnetosonic harmonic separately. Therefore, for respective case the value of T will be determined by the high frequency cut-off of the wave harmonic under study. It may be noted that the resultant vector $\vec{R} = \vec{B}_{w\perp}(t) \times \vec{B}_{w\perp}(t + \Delta t)$ will be perpendicular to the plane containing $\vec{B}_{w\perp}$, hence, it will be either parallel or anti-parallel to $\vec{B}_{w\parallel}$. Therefore, we have defined angle β as a measure of the polarization as follows:

$$\cos(\beta) = \begin{bmatrix} \frac{\vec{B}_0}{|\vec{B}_0|} \\ \frac{\vec{B}_0}{|\vec{R}|} \end{bmatrix} \cdot \begin{bmatrix} \frac{\vec{R}}{|\vec{R}|} \\ \frac{\vec{R}}{|\vec{R}|} \end{bmatrix}$$
(4)

When angle β is zero then the polarization is right-handed and if β is 180°, then the polarization is left-handed. We have also estimated the eccentricity of the observed wave. It is a measure of the elliptical shape made by the perpendicular vector during its rotation in a plane perpendicular to the ambient magnetic field. Eccentricity can vary between 0 and 1. We know that the ellipticity is defined as $\sqrt{1-b^2/a^2}$, where a and b are the semi-major and semi-minor axes of the ellipse, respectively. We have estimated the minimum and maximum amplitudes of the perpendicular wave vector over a T/2 period and computed the eccentricity by making use of the following equation:

$$e = \sqrt{1 - \frac{|\overrightarrow{B}_{w\perp}|_{\min}^2}{|\overrightarrow{B}_{w\perp}|_{\max}^2}} \tag{5}$$

We know that $\nabla \cdot \vec{B}_w = 0$, therefore $\vec{k} \cdot \vec{B}_w = 0$. It suggests that wave vector \vec{k} and the wave magnetic field vector \vec{B}_w are orthogonal to each other. Let us define a vector $\vec{P} = \vec{B}_w(t) \times \vec{B}_w(t + \Delta t)$. Here, a unit vector $\vec{P}/|\vec{P}|$ will point in the direction of the wave vector \vec{k} . We used this information to determine the wave normal angle θ , an angle between the ambient magnetic field and the wave vector \vec{k} , by using the following equation:

$$\theta = \cos^{-1} \left[\frac{\overrightarrow{B}_0}{|\overrightarrow{B}_0|} \right] \cdot \left[\frac{\overrightarrow{B}_w(t) \times \overrightarrow{B}_w(t + \Delta t)}{|\overrightarrow{B}_w(t) \times \overrightarrow{B}_w(t + \Delta t)|} \right]$$
(6)

All the above-mentioned parameters, namely β , e, and θ are determined separately for the fundamental mode and higher frequency harmonics. The distributions of polarization, eccentricity, and wave normal angle are compiled in Table 1 for the magnetosonic wave and its harmonics. It may be noted that in the case of the Earth, at a given location, the direction of the ambient magnetic field can be determined with certainty. It is because the Earth possesses the intrinsic strong magnetic field of definite configuration. However, in the case of Mars, the direction of the ambient magnetic field cannot be determined with certainty as it is an unmagnetized planet and possesses a

KAKAD ET AL. 6 of 14

Table 1

Percentage of Left-Handed and Right-Handed Polarization, Average Eccentricity and Wave Normal Angle for the Fundamental Mode and High Frequency Harmonics of the Magnetosonic Wave at Every 20 min of Interval During the Observed Wave Event

Frequency (Hz)	Start time (UT hours)	End time	LH polarization (%)	RH polarization (%)	$\langle e \rangle$	θ (deg.)
Fundamental mode $(f_0 = 0.01-0.05)$	19.0873	19.4208	92.89	07.11	0.83 ± 0.12	141°
	19.4206	19.7541	77.82	22.18	0.83 ± 0.14	128°
	19.7540	20.0875	48.12	51.88	0.95 ± 0.10	91°
	20.0873	20.4208	88.28	11.72	0.91 ± 0.09	137°
	20.4206	20.7576	87.55	12.45	0.85 ± 0.12	134°
1st harmonic ($f_1 = 0.06-0.12$)	19.7540	20.0875	45.56	54.44	0.86 ± 0.14	90°
2nd harmonic ($f_2 = 0.12-0.16$)	19.7540	20.0875	26.78	73.22	0.85 ± 0.12	70°
3rd harmonic ($f_3 = 0.16-0.2$)	19.7540	20.0875	13.74	86.26	0.86 ± 0.11	55°

Note. The start time and end time over which the information has been quantified are also listed.

weak crustal magnetic field. The observed magnetic field has a contribution from the ambient magnetic field and the wave magnetic field, that is, $B(r,t) = B_0(r,t) + B_w(r,t)$. In such a scenario, we took the average of the observed magnetic field as a proxy to represent the slowly varying ambient magnetic field. The average is estimated over a period of 10 min. The process of averaging nullifies the fluctuations associated with the wave, and we get a slowly varying ambient magnetic field.

One example of the left-handed polarization is shown in Figure 4a. The anti-clockwise rotation of the perpendicular wave vector over 20 s is clearly seen in this plot. Each blue arrow represents the $\overrightarrow{B}_{w\perp}$ for one second, starting from time 10.504 UT. The black arrow represents the direction of the ambient magnetic field. We divided the observation period 19.01–20.7 into five equal intervals of around 20 min, and computed angle β to check the polarization of wave for the fundamental mode. The percentage of left-hand and right-hand polarization is plotted in Figure 4c. It is found that for most of the time, the fundamental mode was associated with the left-handed polarization but during the time of occurrence of harmonics, the wave is found to be associated with both the right- and left-handed polarizations. The harmonics of magnetosonic wave are mostly associated with right-handed polarization. Overall, for the fundamental mode, the total percentage of right- and left-handed polarization is 80% and 20%, respectively. The eccentricity and wave normal angle are shown in Figures 4b and 4d, respectively, as a function of time. The red curves in Figures 4b and 4d give the average value of the respective parameter for every 20 min. We can see that the eccentricity mainly lies between 0.8 and 1, and it is nearly one during the time when magnetosonic harmonics are seen. Similarly, wave normal angle θ is mainly between 150 and 180°, but it changes to 90 and 100° during the time when magnetosonic harmonics are seen.

In Figures 5a and 5b, we have shown the wave angle θ and polarization (i.e., angle β) as a function of frequency and time. Here, first we filtered the original signal into different frequency bins starting from 0.01 to 0.4 Hz by choosing a frequency bin of 0.005 Hz. It gives the lower frequency cut-off as $f_{low} = [0.01:0.005:0.4]$ and upper frequency cut-off is considered as $f_{high} = f_{low} + 0.01$. We have total 78 frequency bins, for which filtered signals were obtained. We choose $\Delta t = T/2$, where, T is chosen as the smallest period that is, the wave period associated with the highest frequency (0.4 Hz). By using Equations 4 and 6, we have computed polarization (β) and wave angle (θ). In Figure 5, the polarization and wave normal angle has a frequency and time resolution of 0.01 Hz and 1 s. This plot clearly indicates that the fundamental mode is associated with the left-handed polarization with a wave propagation angle between 160 and 180° and an eccentricity of 0.8–1 in absence of the harmonics. In contrast, at the time of occurrence of harmonics the magnetosonic wave is mainly associated with right-handed polarization with a wave propagation angle between 60 and 90 and an eccentricity of around 1.

In order to check the wave propagation scenario further, we estimated the average direction of (i) ambient magnetic field, (ii) solar wind velocity, and (iii) wave vector during the wave observation period of $t_{\text{start}} = 19.1$ to $t_{\text{end}} = 20.7$ UT. These vectors are estimated over every 20 min of interval for the fundamental mode, and plotted in Figure 6a. The yellow and gray-shaded portions of the globe indicate the day and night sectors of the Mars. From

KAKAD ET AL. 7 of 14

21699402, 2024, 7, Downloaded from https://agupubs. onlinelibrary.wiley.com/doi/10.1029/2024/A032538 by University Of California - Berkeley, Wiley Online Library on [14/07/2024]. See the Terms and Condit

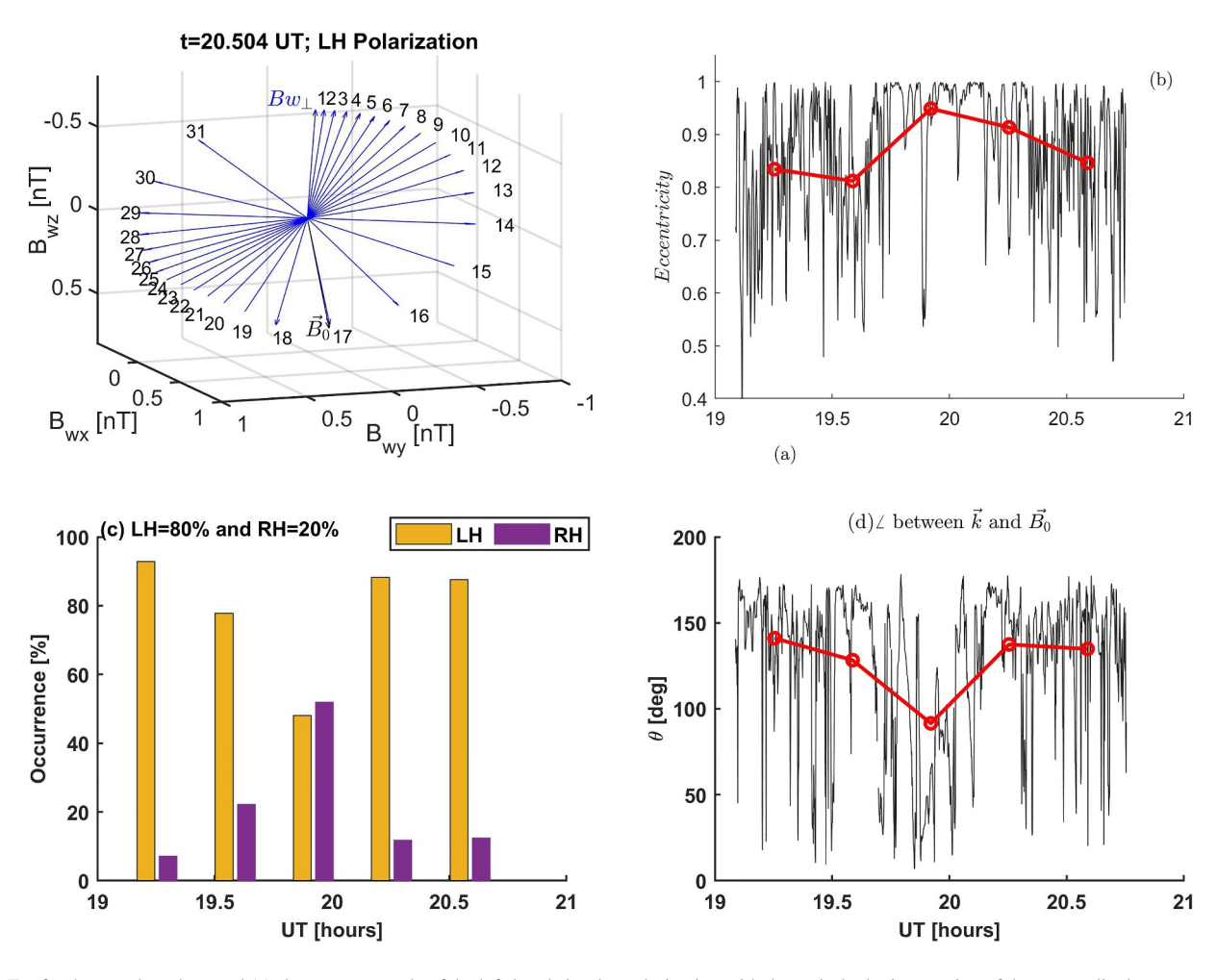


Figure 4. For fundamental mode, panel (a) shows an example of the left-hand circular polarization with the anti-clockwise rotation of the perpendicular wave vector over 20 s, defined with respect to the ambient magnetic field, depicted by a black arrow. Each blue arrow represents the $\vec{B}_{w\perp}$ for one second, starting from time 10.504 UT. Panel (b) depicts the eccentricity as a function of time. Panel (c) displays the percentage of left-hand and right-hand polarization for every 20 min during the occurrence of fundamental wave mode during the time period of 19.1–20.7 UT. Panel (d) indicates the wave normal angle θ as a function of time. The red curves in panels (b, d) represent the average value of the respective parameter for every 20 min.

this Figure 6, we can conclude that the ambient magnetic field and solar wind flow are nearly opposite to each other, and during the time of harmonics the fundamental mode is propagating nearly quasi-perpendicular to the ambient magnetic field away from Mars. These scenarios are illustrated in the form of a schematic in Figures 6b and 6c. The magnetosonic waves are believed to propagate perpendicular to the ambient magnetic field with the characteristics of right-handed polarization (Laakso et al., 1990; Xiao et al., 2014). The polarization and wave vector characteristics estimations for the wave are in good agreement with the earlier studies.

3.3. Validation Through Simulations and Theory

In this section, we describe the results of one-dimensional Particle-In-Cell (PIC) electromagnetic simulations that are performed to understand the generation mechanism of the magnetosonic wave and its harmonics in the weak magnetic field around Mars. For this purpose, we have examined the ambient plasma parameters. The ambient magnetic field, solar wind velocity, proton density, and proton temperature are available at a sampling rate of 4 s. These are the key parameters derived from different instruments on MAVEN and readily available to the scientific community for scrutiny. During the time of wave event, for every 20 min, the average value of each physical parameter is computed and listed in Table 2. It is to be noted that the magnetic field is ≈ 3.3 nT, the proton temperature is ≈ 5 eV, and proton density is ≈ 20 cm⁻³ during the wave observation period. The SWEA instrument shows a peak in the electron flux around few tens of eV, implying that the electron temperature is to be taken as

KAKAD ET AL. 8 of 14

21699402, 2024, 7, Downloaded from https://agupubs.

wiley.com/doi/10.1029/2024JA032538 by University Of California - Berkeley, Wiley Online Library on [14/07/2024]. See the

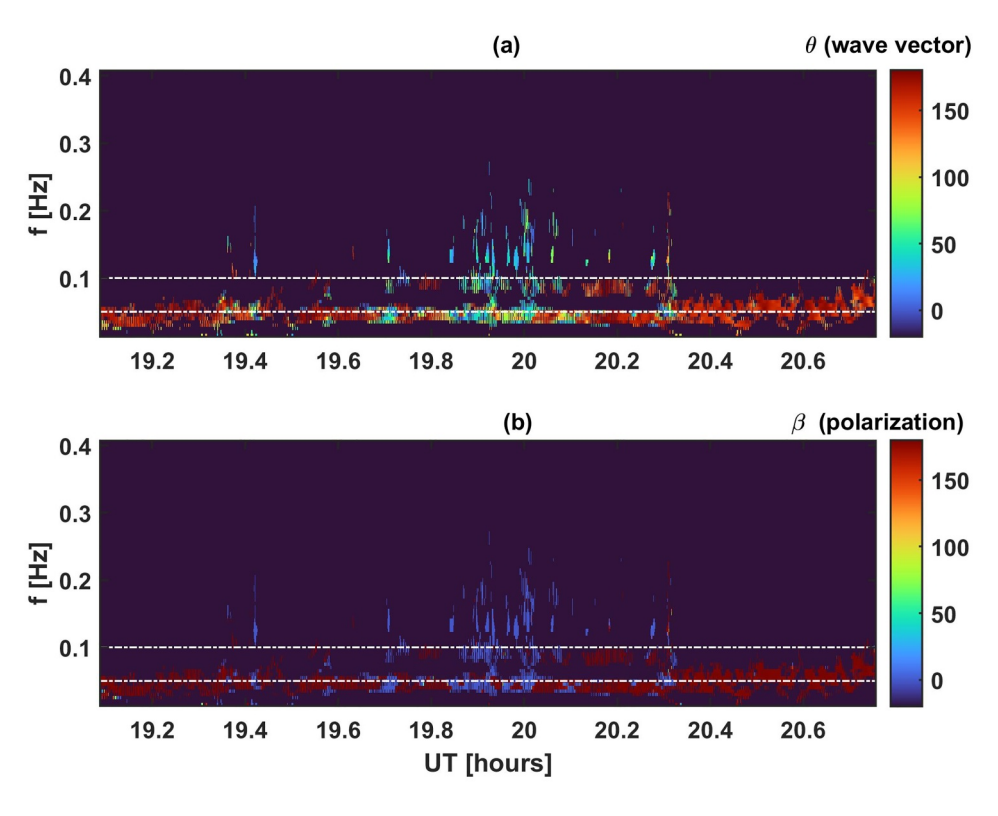


Figure 5. Panel (a) shows the wave normal angle θ , while panel (b) plots angle β , a measure of polarization, as a function of frequency and time.

~10 eV. By considering the quasi-neutrality, we can equate electron and ion densities. These ambient plasma parameters indicate that thermal velocity of electron is $V_{te} = 1,326$ km/s, thermal velocity of ions $V_{ti} = 22$ km/s, $n_i = n_e = n_0 = 20 \times 10^6$ m⁻³, ion plasma frequency is 5.6×10^3 rad/s, electron plasma frequency is 2.5×10^5 rad/s, ion cyclotron frequency is $\omega_{ci} = 0.3$ rad/s, and lower hybrid frequency is 13 rad/s. The magnetosonic waves are observed between the proton gyro-frequency up to lower hybrid frequency. Here, the ratio of ion plasma frequency to ion cyclotron frequency is high due to weak ambient magnetic field. The Debye scale of ions and electrons is around 4–5 m, and the proton gyro-radius is of the order of 100 km. In order to simulate such a plasma system, one needs to choose a smaller grid size to compensate for the Debye scale and a larger system length to compensate for the gyro-radius; therefore, such kinetic simulation becomes computationally expensive. We have used the reduced mass ratio in the simulations to have reasonable computation time. The use of reduced mass ratio does not affect the physical results of the simulation (Matsumoto & Omura, 1993). The magnetosonic waves are linked to ion dynamics and the wave modes involving electron dynamics such as lower hybrid waves are well above those of the dominant harmonics of magnetosonic waves. The normalized mass ratio used in the simulations (i.e., $m_i/m_e = 100$) gives the lower hybrid frequency of 0.1, which is 10 times greater than the ion cyclotron frequency considered in simulations. This justifies the use of reduced mass ratio.

During the time of wave observation the plasma beta, which is the ratio of the thermal pressure to the magnetic pressure, is found to be around 6 and the ratio of electron plasma frequency to gyro frequency is 430, which is very high. In the case of the Earth's magnetosphere, we mostly observe low plasma beta (Boldyrev et al., 2021). In the case of the solar wind plasma near the Earth's bow shock region, the plasma beta vary between 0.5 and 1.5 (B. Kakad et al., 2019). In the Martian magnetosphere, the plasma beta is relatively high, and we have performed simulations for such a system. We assume a reduced electron-to-ion mass ratio of 1/100, and the input parameters for the simulations are chosen based on the observed plasma parameters. We have normalized parameters in the simulations. The system length, grid size, and the time step are taken to be Lx = 1,000 along the x-direction, dx = 0.4, dt = 0.015, respectively. The number of superparticles of each species per grid are taken as 4,096. The equations and methods of the simulation model are given in Omura and Usui (2007) and B. Kakad et al. (2014). The simulation code, KEMPO1 is available at http://space.rish.kyoto-u.ac.jp/software/. It may be noted that the

KAKAD ET AL. 9 of 14

/doi/10.1029/2024JA032538 by University Of California - Berkeley, Wiley Online Library on [14/07/2024]. See the Terms

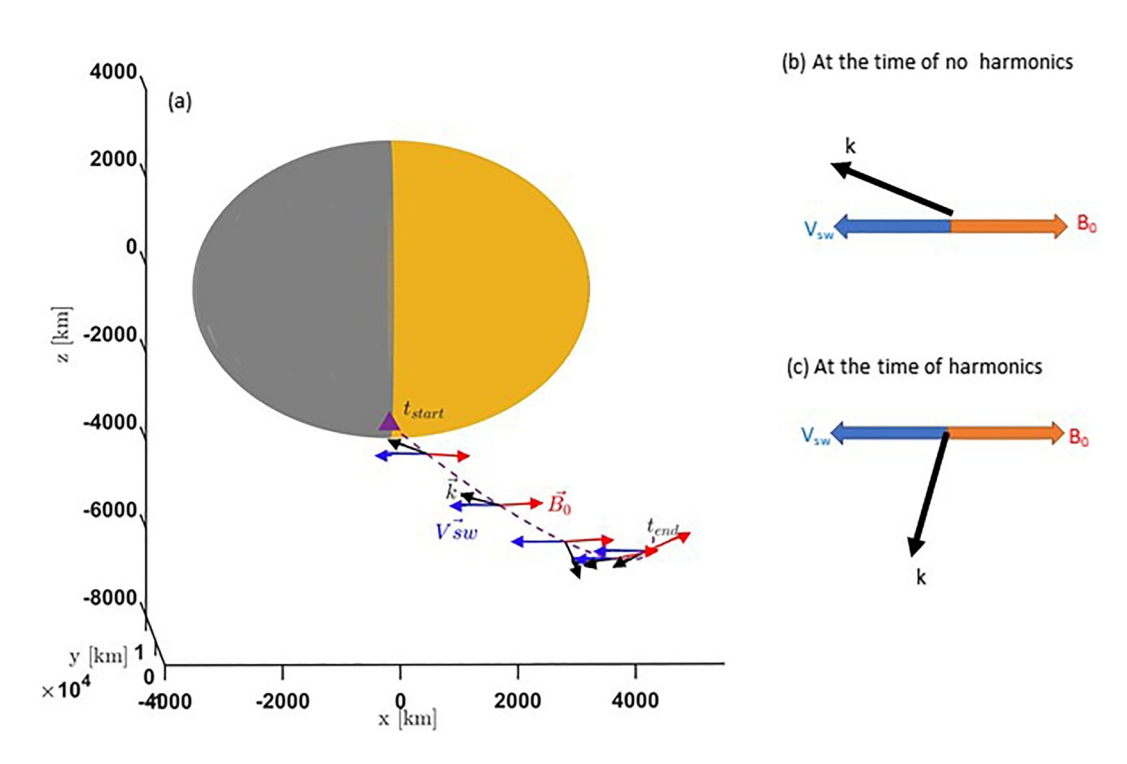


Figure 6. For fundamental mode, the average direction of (i) ambient magnetic field (red arrow), (ii) solar wind velocity (blue arrow), and (iii) wave vector (black arrow) along the trajectory of the MAVEN spacecraft around the Mars during the wave observation period of $t_{\text{start}} = 19.1$ to $t_{\text{end}} = 20.7$ UT hr. Each of these vectors is estimated over every 20 min of interval and plotted accordingly. The yellow and gray-shaded portions of the globe indicate the day and night sectors of Mars. The schematics of the wave vector direction of EMIC wave and magnetosonic wave (defined with respect to the ambient magnetic field and solar wind velocity) are shown in panels (b, c), respectively.

parameters considered in the simulations are normalized. The densities, frequency and velocities are normalized with electron plasma density, electron cyclotron frequency and electron thermal velocity, respectively. The normalized input parameters are sequentially mentioned for [electron, ion, hot ion] as follows; perpendicular thermal velocities $V_{t\perp} = [1, 0.08, 0.08]$, parallel thermal velocities $V_{t\parallel} = [1, 0.08, 0.08]$, density n = [16, 11.2, 4.8], gyro frequencies $\omega_c = [1, 0.01, 0.01]$. The ambient magnetic field is in y-direction. Studies have shown that in Earth's plasmasphere the excitation of the magnetosonic waves is supported by the unstable ring type distribution (Claudepierre et al., 2021). A recent study from Martian ionosphere suggests that ring beam hot proton distributions generated through the penetration of magnetosheath protons can excite magnetosonic waves locally (Wang et al., 2023). Therefore, we have assumed a 30% hot population of ring type velocity distribution. The ring-type hot proton population is introduced by considering a beam in a perpendicular direction such that the drift speed is $V_d = [0, 0, 1.5]$. Such a scenario can be anticipated through the presence of some hot proton particle

Table 2Average Ambient Plasma Parameters at Every 20 min of Interval During the Observed Wave Event

t _{start} (UT hours)	$t_{\rm end}$ (UT hours)	B_0 (nT)	V_{sw} (km/s)	$n_i (\mathrm{cm}^{-3})$	T_i (eV)
19.09	19.42	3.2	304.9	21.6	4.3
19.42	19.75	3.3	307.1	21.9	4.5
19.75	20.09	3.3	305.4	21.8	4.4
20.09	20.42	3.1	302.9	22.5	12.6
20.42	20.76	3.6	307.2	21.1	9.1

Note. The start time, end time over which average is taken, ambient magnetic field, solar wind velocity, ion density and ion temperature are listed.

injection in the generation region. It may be noted that the wave event is observed in the dawn to morning sector, where a beam of such protons may be present to excite these waves. It is because the solar wind blows across the Mars in the dawn and dusk sectors.

The $\omega-k$ plot of the electric field E_z and magnetic field B_y are shown in Figure 7. It is clearly seen that several harmonics of magnetosonic waves are generated in the simulation system at multiples of ω_{ci} by considering a hot population of ions with ring-type velocity distribution. It indicates that generation of harmonics of magnetosonic waves is possible in the plasma environment around Mars, provided there exists a free energy source (in the present PIC simulation, the free energy is assumed by the presence of a ring-type of hot protons). The generation of magnetosonic harmonics has been reported in the literature through simulations in the Earth's magnetosphere (Liu et al., 2011), where the ambient magnetic field is strong. The present

KAKAD ET AL. 10 of 14

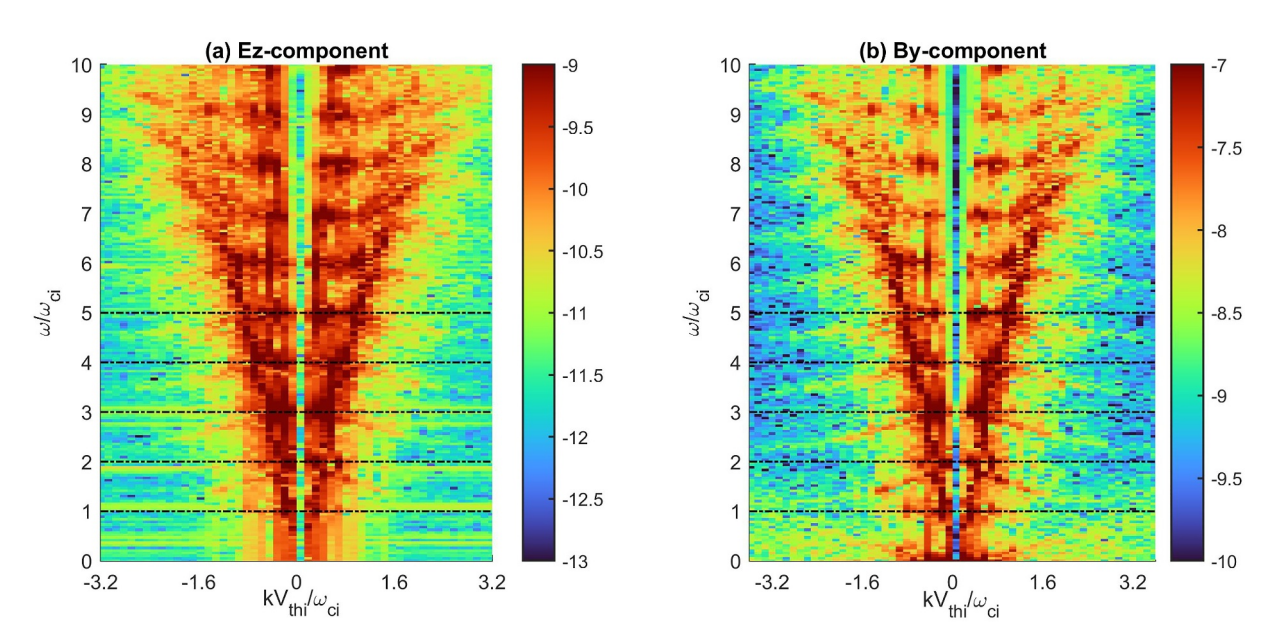


Figure 7. ω -k spectra of E_z and B_y components of electric field and magnetic field, respectively obtained from the PIC simulation during $\omega_{ce}t = 0$ –12,000. The wave vector \vec{k} is in the x-direction. The ambient magnetic field is in the y-direction. The black horizontal dashed lines indicate the multiples of proton gyro-frequency at ω_{ci} , $2\omega_{ci}$, $3\omega_{ci}$, and so on.

simulation shown here is applicable for the weak magnetic field plasma environment. As the purpose of the present paper is to demonstrate a possible scenario of multiple-harmonic proton cyclotron frequency modes in the magnetosonic mode branch, we have focused on the perpendicular propagation.

To interpret the simulation result, let us consider the linear stability of the proton ring velocity distribution function. For the sake of simplicity, we restrict ourselves to the exactly perpendicular propagation, which the present PIC simulation also assumed. To simplify the problem further, we assume a quasi-electrostatic approximation. As we are only concerned with the low frequency and long-wavelength modes, we may ignore the electron dynamics. Then one can show that the dispersion relation for quasi electrostatic mode propagating in perpendicular direction with respect to the ambient magnetic field is given by (Lee & Birdsall, 1979; Tataronis & Crawford, 1970),

$$0 = 1 - \frac{2\pi\omega_{pi}^2}{k_\perp^2} \int_0^\infty d\nu_\perp \left(1 - J_0^2(b) - \sum_{n=1}^\infty \frac{2\omega^2 J_n^2(b)}{\omega^2 - n^2 \Omega_i^2} \right) \frac{\partial f_i(\nu_\perp)}{\partial \nu_\perp},$$

$$b = \frac{k_\perp \nu_\perp}{\Omega_i}.$$
(7)

Here, $\Omega_i = eB_0/m_ic$ is the ion (proton) cyclotron frequency with e, B_0 , m_i , and c denoting the unit electric charge, the ambient magnetic field intensity, proton mass, and the speed of light, respectively. The ion plasma frequency ω_{pi} is defined as $\omega_{pi}^2 = 4\pi n_0 e^2/m_i$, where n_0 is the ambient proton density. As for the proton velocity distribution function, f_i , we adopt the thermal ring model (Yoon et al., 2014),

$$f_i(v_\perp) = \frac{1}{\pi \alpha^2 A} \exp\left(-\frac{(v_\perp - v_0)^2}{\alpha^2}\right),$$

$$A = 2\int_0^\infty dx x e^{-(x-u)^2}, \qquad u = \frac{v_0}{\alpha}.$$
(8)

An example of the wave dispersion relation is shown in Figure 8. Blue curves are real frequencies and red curves denote the growth rates for multiple-harmonic proton-cyclotron modes. The unstable portions of the real frequencies are plotted with thicker lines to facilitate the visual identification of the structure of unstable modes. In

KAKAD ET AL.

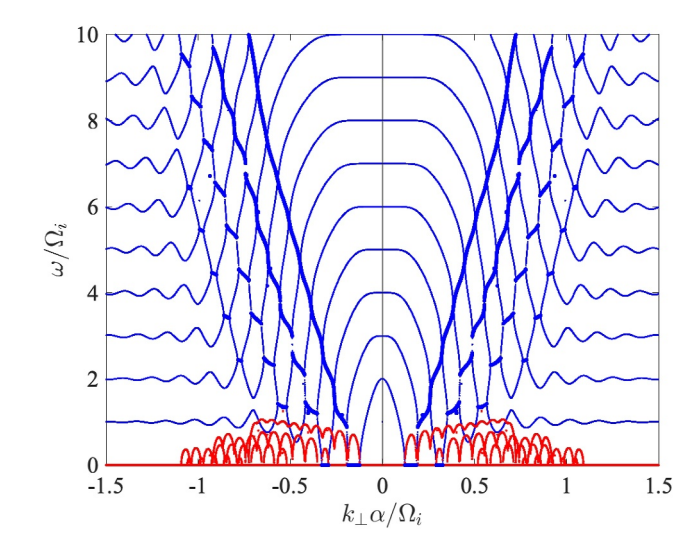


Figure 8. An example of the quasi-electrostatic ion Bernstein mode dispersion relation, which is a limiting case of multiple-harmonic magnetosonic mode for perpendicular propagation.

generating Figure 8 we have adopted the dimensionless proton ring speed, which is taken to be consistent with that of the PIC simulation, namely, $v_0/\alpha \sim$ 20. Here, α is thermal velocity and v_0 is beam speed of hot protons. The other dimensionless parameter that determines the dispersive property is ω_n/Ω_i , which we chose to be 40. Figure 8 shows that multiple-harmonic proton cyclotron modes are excited up to tenth harmonics or higher. Note that the overall mode structure is similar to that of the classic works that may be found in the literature, for example, electron cold ring-driven Bernstein mode instability (Tataronis & Crawford, 1970) and the proton cold ring-driven ion Bernstein mode instability (Lee & Birdsall, 1979). The main difference between these works and the present model is that we have adopted the thermal ring distribution as compared with the delta-function ring distribution f $(v_{\perp}) \propto \delta(v_{\perp} - v_0)$. Note that a similar thermal electron ring model was also considered in a relatively recent work (Yoon et al., 2014), but the application to the proton thermal ring model has not been carried out until now. In any event, the present linear theory is largely consistent with our PIC simulation, in that one can see that the multiple-harmonic proton-cyclotron modes form a quasi-continuous curve up the chain of cyclotron harmonics with increasing wavenumber as the frequency increases. This is superficially similar to the simulation result—see in particular, E_7 plot in Figure 7.

4. Summary and Conclusions

In this article, we report the first observation of the harmonics of a magnetosonic wave in the vicinity of unmagnetized planet Mars. The generation of harmonics of magnetosonic waves has been confirmed by simulations and theory by assuming that a suitable free energy source is present. In the present case, we have assumed that a population of hot protons with a velocity-space ring feature along the perpendicular direction is present. The harmonics of magnetosonic wave are observed in the Martian magnetosphere in the dawn-to-morning sector at around 5–10 LT. The magnetosonic harmonics are observed below ion cyclotron wave at f_{ci} , however by considering the Doppler shift this wave is identified as the fundamental mode. The proton cyclotron frequency is approximately 46 mHz. The fundamental mode of magnetosonic wave is dominated by the left-handed polarization, whereas the higher frequency harmonics are mainly associated with right-handed polarization. The ambient proton density and velocity are found to vary with the proton cyclotron frequency of 46 mHz. During these wave observations, the ambient magnetic field and solar wind flow are nearly opposite to each other. The magnetosonic wave harmonics are propagating quasi-perpendicular to the ambient magnetic field.

Wang et al. (2023) and Teng et al. (2024) have reported magnetosonic waves in the Martian upper atmosphere. Teng et al. (2024) observed magnetosonic emissions close to proton gyro-frequency in the magnetotail region of the Mars and these waves were associated with significant increase in proton and oxygen fluxes. In the present study, the magnetosonic wave amplitude is around 3 nT, which is comparable to the wave amplitude observed in the Martian ionosphere (Wang et al., 2023). The wave frequency observed in the Martian ionosphere is in the frequency range of 0.2–1 Hz, whereas it is 0.2–0.5 Hz in the Martian magnetotail and these waves are found to be highly oblique to the ambient magnetic field. This indicates that the observed frequency range and characteristics of the magnetosonic wave harmonics in the Martian magnetosheath presented in this paper is in agreement with earlier studies. Recent studies have shown that both magnetosonic waves and EMIC waves could be simultaneously generated by a ring-type proton distribution in the Earth's inner magnetosphere (Min & Liu, 2016; Teng, Ma, & Tao, 2021). In the Earth's magnetosphere, the typical frequency of the Magnetosonic waves and EMIC waves are found to be in the range of 10–100 Hz and 1–10 Hz, respectively. In the present study, the magnetosonic wave harmonics are observed in magnetosheath region of Mars and frequency is below 0.4 Hz. In the present observation, the Doppler shift cannot be neglected and therefore the mode that appears below f_{ci} is identified as the fundamental mode of magnetosonic wave.

The harmonics of magnetosonic waves have been extensively observed in the Earth's magnetosphere (Balikhin et al., 2015; Huang et al., 2020). In comparison with the Earth, the magnetic field on Mars is very weak. In such a tenuous magnetic field environment, the occurrence of the harmonics of a magnetosonic wave has not been reported so far. The present study provides evidence for the generation of harmonics of magnetosonic waves in

KAKAD ET AL. 12 of 14

Wiley Online Library on [14/07/2024]. See the Terms

the Martian bow shock-magnetosheath region. As these waves are known to play an important role in particle heating in the generation region (Horne et al., 2000), they can have similar implications for the Martian magnetosphere. We have observed the magnetosonic wave in the dawn sector of Mars at an altitude of 4,000–6,000 km. As the solar wind encounters Mars and flows around it, one can assume that the presence of a hot proton population in this region can provide the hot ring-type distribution, which is needed to excite the magnetosonic wave. Simulations performed here indicate that by taking into account the population of hot protons of ring-type distribution along with the cold protons can generate harmonics of a magnetosonic wave in the presence of weak magnetic field.

Data Availability Statement

The data used in the present study are available on the Planetary Data System (https://pds-ppi.igpp.ucla.edu/). The simulation code, KEMPO1 is available at http://space.rish.kyoto-u.ac.jp/software/.

Acknowledgments References

The authors thank J.E.P. Connerney for providing access to MAG/MAVEN data, D.L.Mitchell for SWEA/MAVEN data and J.S. Halekas for SWIA/MAVEN data and P.A., Dunn for key parameters. AK and BK acknowledges research funding project IIG/EPTOS and IIG/MI-PEARL. YO was supported by JSPS KAKENHI Grants JP23H05429 and JP24K00691. PHY acknowledges NSF Grant 2203321, NASA Grant 80NSSC23K0662, and DOE (FES) Award DE-SC0022963 through the NSF/DOE Partnership in Basic Plasma Science and Engineering to the University of Marvland.

- Andersson, L., Ergun, R., Delory, G., Eriksson, A., Westfall, J., Reed, H., et al. (2015). The Langmuir probe and waves (LPW) instrument for maven. Space Science Reviews, 195(1), 173–198. https://doi.org/10.1007/s11214-015-0194-3
- Balikhin, M. A., Shprits, Y. Y., Walker, S. N., Chen, L., Cornilleau-Wehrlin, N., Dandouras, I., et al. (2015). Observations of discrete harmonics emerging from equatorial noise. *Nature Communications*, 6(1), 7703. https://doi.org/10.1038/ncomms8703
- Bertucci, C., Mazelle, C., Crider, D., Mitchell, D., Sauer, K., Acuña, M., & Winterhalter, D. (2004). MGS MAG/ER observations at the magnetic pileup boundary of Mars: Draping enhancement and low frequency waves. *Advances in Space Research*, 33(11), 1938–1944. https://doi.org/10.1016/s0273-1177(04)00034-1
- Boldyrev, S., Loureiro, N. F., & Roytershteyn, V. (2021). Plasma dynamics in low-electron-beta environments. Frontiers in Astronomy and Space Sciences, 8, 621040. https://doi.org/10.3389/fspas.2021.621040
- Chen, L., Thorne, R. M., Jordanova, V. K., Thomsen, M. F., & Horne, R. B. (2011). Magnetosonic wave instability analysis for proton ring distributions observed by the LANL magnetospheric plasma analyzer. *Journal of Geophysical Research*, 116(A3). https://doi.org/10.1029/ 2010ia016068
- Claudepierre, S. G., Liu, X., Chen, L., & Takahashi, K. (2021). Observational evidence of the excitation of magnetosonic waves by an He⁺⁺ ion ring distribution. *Journal of Geophysical Research: Space Physics*, 126(8), e2021JA029532. https://doi.org/10.1029/2021ja029532
- Collinson, G., Wilson III, L. B., Omidi, N., Sibeck, D., Espley, J., Fowler, C. M., et al. (2018). Solar wind induced waves in the skies of mars: Ionospheric compression, energization, and escape resulting from the impact of ultralow frequency magnetosonic waves generated upstream of the Martian bow shock. *Journal of Geophysical Research: Space Physics*, 123(9), 7241–7256. https://doi.org/10.1029/2018ja025414
- Connerney, J., Espley, J., Lawton, P., Murphy, S., Odom, J., Oliversen, R., & Sheppard, D. (2015). The maven magnetic field investigation. *Space Science Reviews*, 195(1), 257–291. https://doi.org/10.1007/s11214-015-0169-4
- DiBraccio, G. A., Luhmann, J. G., Curry, S. M., Espley, J. R., Xu, S., Mitchell, D. L., et al. (2018). The twisted configuration of the Martian magnetotail: Maven observations. *Geophysical Research Letters*, 45(10), 4559–4568. https://doi.org/10.1029/2018gl077251
- Ergun, R., Andersson, L., Fowler, C., Woodson, A., Weber, T., Delory, G., et al. (2016). Enhanced O₂⁺ loss at mars due to an ambipolar electric field from electron heating. *Journal of Geophysical Research: Space Physics*, 121(5), 4668–4678. https://doi.org/10.1002/2016ja022349
- Ergun, R., Andersson, L., Peterson, W., Brain, D., Delory, G., Mitchell, D., et al. (2006). Role of plasma waves in mars' atmospheric loss. Geophysical Research Letters, 33(14). https://doi.org/10.1029/2006gl025785
- Espley, J., Cloutier, P., Brain, D., Crider, D., & Acuña, M. (2004). Observations of low-frequency magnetic oscillations in the Martian magnetosheath, magnetic pileup region, and tail. *Journal of Geophysical Research*, 109(A7). https://doi.org/10.1029/2003ja010193
- Fowler, C., Agapitov, O., Xu, S., Mitchell, D., Andersson, L., Artemyev, A., et al. (2020). Localized heating of the Martian topside ionosphere through the combined effects of magnetic pumping by large-scale magnetosonic waves and pitch angle diffusion by whistler waves. Geophysical Research Letters, 47(5), e2019GL086408. https://doi.org/10.1029/2019g1086408
- Fowler, C., Andersson, L., Ergun, R., Harada, Y., Hara, T., Collinson, G., et al. (2018). Maven observations of solar wind-driven magnetosonic waves heating the Martian dayside ionosphere. *Journal of Geophysical Research: Space Physics*, 123(5), 4129–4149. https://doi.org/10.1029/ 2018ia025208
- Gary, S. P., Liu, K., Winske, D., & Denton, R. E. (2010). Ion Bernstein instability in the terrestrial magnetosphere: Linear dispersion theory. Journal of Geophysical Research, 115(A12). https://doi.org/10.1029/2010ja015965
- Guo, Z., Liu, Y., Fu, H., Cao, J., Xu, Y., Wang, Z., et al. (2022). First observation of lower hybrid drift waves at the edge of the current sheet in the Martian magnetotail. *The Astrophysical Journal*, 933(2), 128. https://doi.org/10.3847/1538-4357/ac722b
- Halekas, J., Brain, D., & Eastwood, J. (2011). Large-amplitude compressive "sawtooth" magnetic field oscillations in the Martian magnetosphere. Journal of Geophysical Research, 116(A7). https://doi.org/10.1029/2011ja016590
- Halekas, J., Ruhunusiri, S., Harada, Y., Collinson, G., Mitchell, D., Mazelle, C., et al. (2017). Structure, dynamics, and seasonal variability of the mars-solar wind interaction: Maven solar wind ion analyzer in-flight performance and science results. *Journal of Geophysical Research: Space Physics*, 122(1), 547–578. https://doi.org/10.1002/2016ja023167
- Halekas, J., Taylor, E., Dalton, G., Johnson, G., Curtis, D., McFadden, J., et al. (2015). The solar wind ion analyzer for maven. Space Science Reviews, 195(1), 125–151. https://doi.org/10.1007/s11214-013-0029-z
- Harada, Y., Andersson, L., Fowler, C., Mitchell, D., Halekas, J., Mazelle, C., et al. (2016). Maven observations of electron-induced whistler mode waves in the Martian magnetosphere. *Journal of Geophysical Research: Space Physics*, 121(10), 9717–9731. https://doi.org/10.1002/2016ja023194
- Harada, Y., Ruhunusiri, S., Halekas, J., Espley, J., DiBraccio, G., Mcfadden, J., et al. (2019). Locally generated ULF waves in the Martian magnetosphere: Maven observations. *Journal of Geophysical Research: Space Physics*, 124(11), 8707–8726. https://doi.org/10.1029/2019ja027312
- Horne, R. B., Wheeler, G. V., & Alleyne, H. S. C. (2000). Proton and electron heating by radially propagating fast magnetosonic waves. *Journal of Geophysical Research*, 105(A12), 27597–27610. https://doi.org/10.1029/2000ja000018

KAKAD ET AL. 13 of 14

- Huang, S., Deng, D., Yuan, Z., Jiang, K., Li, J., Deng, X., et al. (2020). First observations of magnetosonic waves with nonlinear harmonics. Journal of Geophysical Research: Space Physics, 125(6), e2019JA027724. https://doi.org/10.1029/2019ja027724
- Jian, L., Russell, C., Luhmann, J., Anderson, B., Boardsen, S., Strangeway, R., et al. (2010). Observations of ion cyclotron waves in the solar wind near 0.3 AU. *Journal of Geophysical Research*, 115(A12). https://doi.org/10.1029/2010ja015737
- Kakad, A., Kakad, B., Yoon, P. H., Omura, Y., & Kourakis, I. (2023). Characterization of high-frequency waves in the Martian magnetosphere. Astronomy & Astrophysics, 679, A78. https://doi.org/10.1051/0004-6361/202244756
- Kakad, B., Kakad, A., Aravindakshan, H., & Kourakis, I. (2022). Debye-scale solitary structures in the Martian magnetosheath. The Astrophysical Journal, 934(2), 126. https://doi.org/10.3847/1538-4357/ac7b8b
- Kakad, B., Kakad, A., & Omura, Y. (2014). Nonlinear evolution of ion acoustic solitary waves in space plasmas: Fluid and particle-in-cell simulations. *Journal of Geophysical Research: Space Physics*, 119(7), 5589–5599. https://doi.org/10.1002/2014ja019798
- Kakad, B., Kakad, A., Ramesh, D. S., & Lakhina, G. S. (2019). Diminishing activity of recent solar cycles (22–24) and their impact on geospace. Journal of Space Weather and Space Climate, 9, A1. https://doi.org/10.1051/swsc/2018048
- Kakad, B., Omura, Y., Kakad, A., Upadhyay, A., & Sinha, A. K. (2018). Characteristics of subpacket structures in ground emic wave observations. *Journal of Geophysical Research: Space Physics*, 123(10), 8358–8376. https://doi.org/10.1029/2018ja025473
- Laakso, H., Junginger, H., Roux, A., Schmidt, R., & de Villedary, C. (1990). Magnetosonic waves above fc (H+) at geostationary orbit: GEOS 2 results. *Journal of Geophysical Research*, 95(A7), 10609–10621. https://doi.org/10.1029/ja095ia07p10609
- Lee, J. K., & Birdsall, C. (1979). Velocity space ring-plasma instability, magnetized, Part I: Theory. The Physics of Fluids, 22(7), 1306–1314. https://doi.org/10.1063/1.862733
- Leonovich, A., & Kozlov, D. (2013). Magnetosonic resonances in the magnetospheric plasma. Earth Planets and Space, 65(5), 369–384. https://doi.org/10.5047/eps.2012.07.002
- Liu, K., Gary, S. P., & Winske, D. (2011). Excitation of magnetosonic waves in the terrestrial magnetosphere: Particle-in-cell simulations. *Journal of Geophysical Research: Space Physics*, 116(A7). https://doi.org/10.1029/2010ja016372
- Matsumoto, H., & Omura, Y. (1993). Computer space plasma physics. Terra Scientific Publication Co.
- Meredith, N. P., Horne, R. B., & Anderson, R. R. (2008). Survey of magnetosonic waves and proton ring distributions in the Earth's inner magnetosphere. *Journal of Geophysical Research*, 113(A6). https://doi.org/10.1029/2007ja012975
- Min, K., & Liu, K. (2016). Proton velocity ring-driven instabilities in the inner magnetosphere: Linear theory and particle-in-cell simulations. Journal of Geophysical Research: Space Physics, 121(1), 475–491. https://doi.org/10.1002/2015ja022042
- Mitchell, D., Mazelle, C., Sauvaud, J.-A., Thocaven, J.-J., Rouzaud, J., Fedorov, A., et al. (2016). The maven solar wind electron analyzer. *Space Science Reviews*, 200(1), 495–528. https://doi.org/10.1007/s11214-015-0232-1
- Omura, Y., & Usui, H. (2007). One-dimensional electromagnetic particle code KEMPO1: A tutorial on microphysics in space plasmas. *Advanced*
- methods for space simulations, 1-21.

 Santolík, O., Parrot, M., & Němec, F. (2016). Propagation of equatorial noise to low altitudes: Decoupling from the magnetosonic mode.
- Geophysical Research Letters, 43(13), 6694–6704. https://doi.org/10.1002/2016g1069582

 Su, Z., Liu, N., Gao, Z., Wang, B., Zheng, H., Wang, Y., & Wang, S. (2020). Rapid Landau heating of Martian topside ionospheric electrons by large-amplitude magnetosonic waves. Geophysical Research Letters, 47(20), e2020GL090190. https://doi.org/10.1029/2020gl090190
- Tataronis, J. A., & Crawford, F. (1970). Cyclotron harmonic wave propagation and instabilities: I. Perpendicular propagation. *Journal of Plasma Physics*, 4(2), 231–248. https://doi.org/10.1017/s0022377800004979
- Teng, S., Liu, N., Ma, Q., Tao, X., & Li, W. (2021). Direct observational evidence of the simultaneous excitation of electromagnetic ion cyclotron waves and magnetosonic waves by an anisotropic proton ring distribution. *Geophysical Research Letters*, 48(8), e2020GL091850. https://doi.org/10.1029/2020gl091850
- Teng, S., Ma, Q., & Tao, X. (2021). Simultaneous observations and combined effects of electromagnetic ion cyclotron waves and magnetosonic waves. *Geophysical Research Letters*, 48(16), e2021GL093885. https://doi.org/10.1029/2021gl093885
- Teng, S., Sun, J., Gao, J., Harada, Y., Fraenz, M., & Han, D. (2024). Maven observation of magnetosonic waves in the Martian magnetotail region. Earth and Planetary Physics, 8(2), 317–325. https://doi.org/10.26464/epp2024003
- Wang, J., Yu, J., Chen, Z., Xu, X., Cui, J., & Cao, J. (2023). Local generation of magnetosonic waves by ring beam hot protons in the Martian ionosphere. *Geophysical Research Letters*, 50(9), e2023GL102911. https://doi.org/10.1029/2023g1102911
- Xiao, F., Zong, Q., Wang, Y., He, Z., Su, Z., Yang, C., & Zhou, Q. (2014). Generation of proton aurora by magnetosonic waves. *Scientific Reports*, 4(1), 5190. https://doi.org/10.1038/srep05190
- Yoon, P. H., Hadi, F., & Qamar, A. (2014). Bernstein instability driven by thermal ring distribution. *Physics of Plasmas*, 21(7). https://doi.org/10.1063/1.4887000

KAKAD ET AL. 14 of 14